

Rupture imaging for the 2016 August 24, Mw=6.0 central Italy earthquake, from back-projection of strong-motion array data.

GILBERTO SACCOROTTI, DAVIDE PICCININI AND CARLO GIUNCHI

Istituto Nazionale di Geofisica e Vulcanologia, Sezione di Pisa.

gilberto.saccorotti@ingv.it

Abstract

By extending the conventional Beam-Forming frequency-wavenumber power spectral estimate to the case of arbitrarily-shaped wavefronts, we obtained images of rupture propagation during the 2016 August 24, Mw=6.0 Central Italy earthquake. Using a set of strong-motion accelerometers, we evaluate the beam power along the travel time curves associated with synthetic sources spanning a model fault surface. This allows deriving time-dependent images of the distribution of energy radiation throughout the fault plane. Results indicate bi-lateral rupture propagation toward SE and NW, in rough agreement with surface co-seismic displacement and surface damage pattern. To a first order, our results are also consistent with those obtained from full-waveform inversion of strong-motion data.

I. INTRODUCTION

On August 24, 2016, at 01:36:32 UTC a Mw=6.0 struck the central sector of the Apennines chain (Italy), causing almost 300 casualties and extensive destruction. According to the Time-Domain Moment Tensor (TDMT) solution dispatched by INGV soon after the event, the earthquake was caused by normal faulting with planes striking along the Apennines direction, i.e. SSE-NNW (GdL INGV, 2016; Fig. 1). Subsequent analyses of the GPS and Synthetic Aperture Radar (SAR) deformation patterns [GdL IREA-CNR & INGV, 2016] and aftershocks distribution allow constraining the causative fault to the

south-western-dipping nodal plane of the TDMT solution. This mechanism is consistent with the structural features of this sector of the Apennines, characterized by NNW-SSE-trending, west-dipping extensional Quaternary faults which are responsible for most of the destructive earthquakes that struck Italy over the last decades. In recent years, thanks to the growing availability of data from dense digital networks, back-projection of seismic array data allowed to track rupture propagation for several major earthquakes worldwide (e.g., Kiser and Ishii, 2012; Meng *et al.*, 2012, and references therein). This approach is particularly attractive, as it constrains the spatio-temporal evolution of the rupture solely on the base of

the phase of coherent array signals. Thus, it does not require any detailed knowledge of Green's functions and fault geometry, or restrictive parameterizations of the rupture kinematics. Following these premises, in this note we present time-dependent images of rupture propagation during the 2016, August 24 mainshock by back-projection of P-wave recordings from two set of strong-motion accelerometers. We adopt a standard beamforming procedure (e.g., Abrahamson and Bolt, 1987), which seeks

the maximum power of the recorded seismograms along the travel time curves associated with trial source locations. The method suffers from low resolution, especially in the case of multiple, simultaneously emitting sources (e.g., Goldstein and Archuleta, 1987). Nonetheless, the retrieved pictures are consistent with both the coseismic displacement imaged by satellite interferometry and damage distribution at the surface.

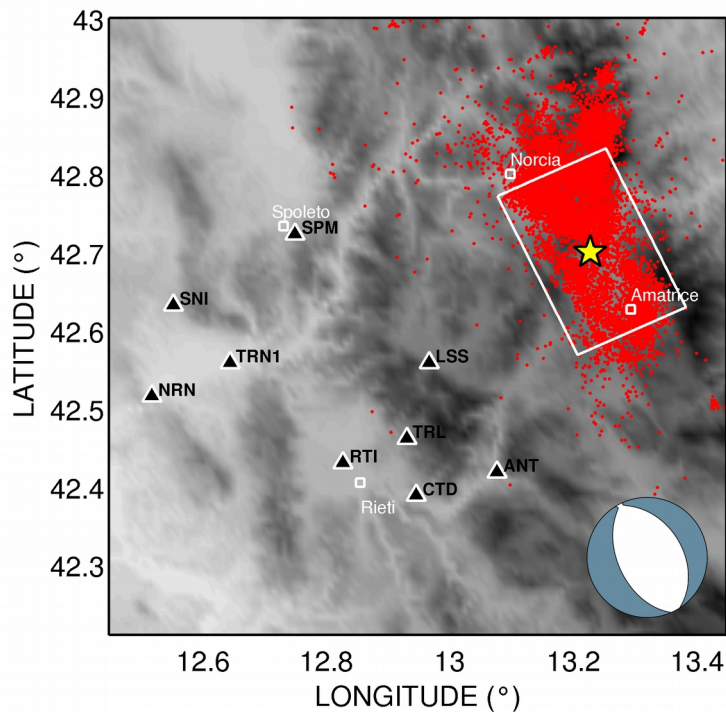


Figure 1 - Map of the study area, with epicentral locations updated to September 25, 2016 (red dots). Black triangles are RAN stations used for the study. The star marks the epicenter of the mainshock, and the white line is the projection of the fault to the surface. The beach ball indicates the focal solution as reported by the TDMT catalog [<http://cnt.rm.ingv.it/tdmt.html>].

II. DATA

For this study we used data from nine stations pertaining to the National Accelerometric Network (hereinafter: RAN), owned and managed

by the Italian Department for Civil Protection (see section on Data and Sharing Resources). These stations are all located west of the fault, at epicentral distances ranging between 26 and 61 km (Fig. 1). Preliminary inspection of the

three-component recordings evidenced that the S-waves suffered important loss of coherence even for small inter-station distances. Moreover, those waves are characterized by a low frequency content (~ 0.3 Hz on velocity seismograms), which make them not appropriate for investigating the dynamical evolution of the source over short time intervals. Due to these reasons, we conducted our analyses only on the P wavetrain as recorded at the vertical components of ground motion. Accelerograms were pre-processed to remove the offset and linear trend, high-pass filtered with a two-pole, single-pass 0.1 Hz Butterworth filter, and finally integrated in time to obtain ground velocity. As for any other array processing scheme, beamforming requires that the wavefield maintains significant coherence among the different array channels. Therefore, we conducted the analysis separately for two sub-arrays, composed by stations [LNS, ANT, CTD, TRL, RTI] and [SPM, TRN, NRN, SNI], hereinafter referred to as sub-arrays AR1 and AR2, respectively (see Fig. 1). The vertical-component seismograms for the mainshock as recorded by the two cluster of stations are illustrated in Figure 2.

III. METHODS

Following hypocentral data and focal mechanisms dispatched by INGV (<http://cnt.rm.ingv.it/event/7073641>; last accessed October 20, 2016), the mainshock's fault is modeled as a 25x16km plane striking 156° and dipping 50° , centered on the catalog hypocenter. This model fault is then discretized using a regular grid of nodes spaced by 0.5km along both the strike and dip directions. For each grid node, we calculate the theoretical travel times to all the array elements using a smoothed version

of the reference 1D model reported by Caranante *et al.* (2013) (Fig. 3).

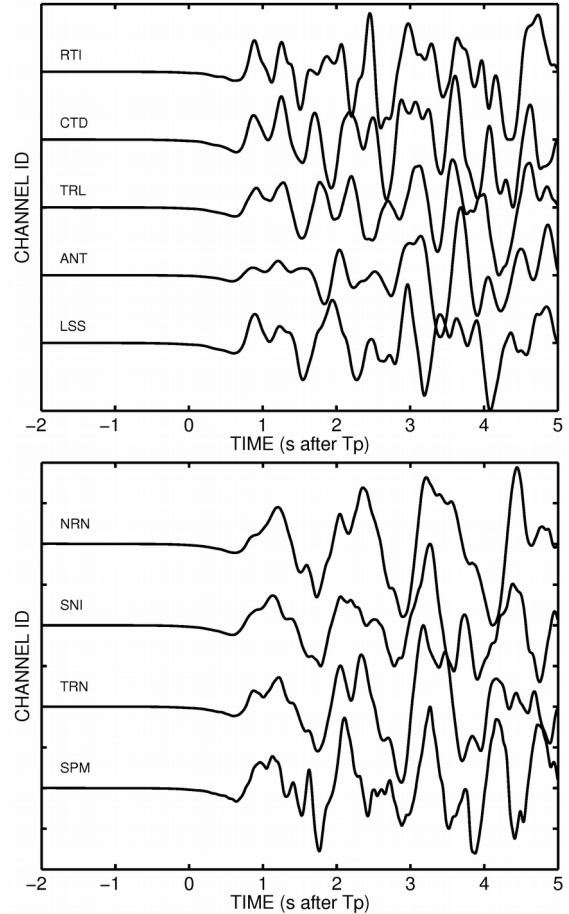


Figure 2 – Vertical-component velocity seismograms from strong-motion accelerometer sub-arrays AR1 (top) and AR2 (bottom), whose location is shown in Fig. 1. Data are band-pass filtered within the 0.5-4Hz frequency band and aligned to the P-wave arrival.

Station residuals are then calculated as the difference between the observed P-wave travel times, and those calculated for the grid node coinciding with the hypocenter. These residuals are then used to derive the corrected travel times Δ' which are stored for the subsequent utilization in beam forming (BF) estimates. The analysis proceeds by aligning the velocity seis-

mograms using the inter-station time differences estimated via cross-correlation to adjust the manually-picked P-wave arrival times.

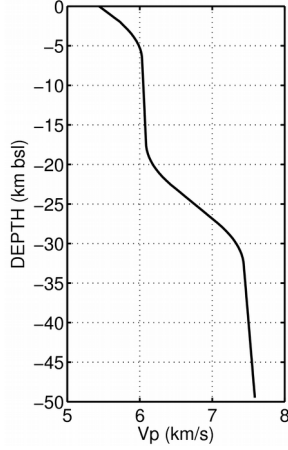


Figure 3 – The P-wave velocity model used for calculating theoretical travel times (after Carannante *et al.*, 2013).

The main advantage of this preprocessing is that it allows for the use of time windows which are shorter than the average propagation time across the array, thus providing more precise estimates of phase differences among array channels (e.g., Goldstein and Archuleta, 1991a). The array seismograms are then used for deriving time-varying estimates of source location on the fault plane using a conventional, frequency-domain beam forming estimator (e.g., Abrahamson and Bolt, 1987; Rost and Thomas, 2002). Separate tests with synthetics (not shown here) demonstrated that this method, though less resolute, provides results which are more reliable than those obtained from much sophisticated approaches such as Capon’s High-Resolution (Capon, 1969) or MUSIC (Goldstein and Archuleta, 1987) estimates. For a given time frame, the evaluation of BF power spectra is conducted through the following steps:

- (a) Fourier transform of the array signal;
- (b) Given a reference frequency ω_0 , calculation of the spatial covariance matrix $\mathbf{R}(\omega_0)$, by smoothing the cross-spectral estimates over the three frequency bins centered at ω_0 (eq. 21 in Abrahamson and Bolt, 1987);
- (c) For each fault grid node located at \mathbf{X} , calculation of the array steering vector \mathbf{A} whose elements are given by:

$$a_i(\omega_0, \mathbf{X}) = \exp[-i \omega_0 \Delta'(\mathbf{X}, \mathbf{x}_i) - T_i] \quad i=1, \dots, N \quad (1)$$

where Δ' and T are the theoretical and observed travel times, respectively, \mathbf{x} is the position vector of the generic array element, and N is the number of stations. Once applied to the cross-spectral matrix, these terms have the effect of shifting the phase of the estimated spatial cross-spectra according to what predicted for a generic source located at \mathbf{X} .

- (d) Estimate of the BF power spectral estimator which, in matrix notation, is written as:

$$P(\mathbf{X}) = \mathbf{A}^H \mathbf{R} \mathbf{A} \quad (2)$$

where the H superscript indicates the complex conjugate transpose. When \mathbf{X} coincides with the true source location, all the array cross-spectra in \mathbf{R} are brought in phase by the operator \mathbf{A} , and their squared sum (i.e., the beam power P) will thus take a maximum. Steps (b-d) are repeated for all the discrete frequencies spanning the 0.5-4 Hz frequency band, and a final broad-band power spectrum is obtained by linearly stacking the narrow-band BF spectra (eq. 2) obtained at individual frequency bins (Gal *et al.*, 2014).

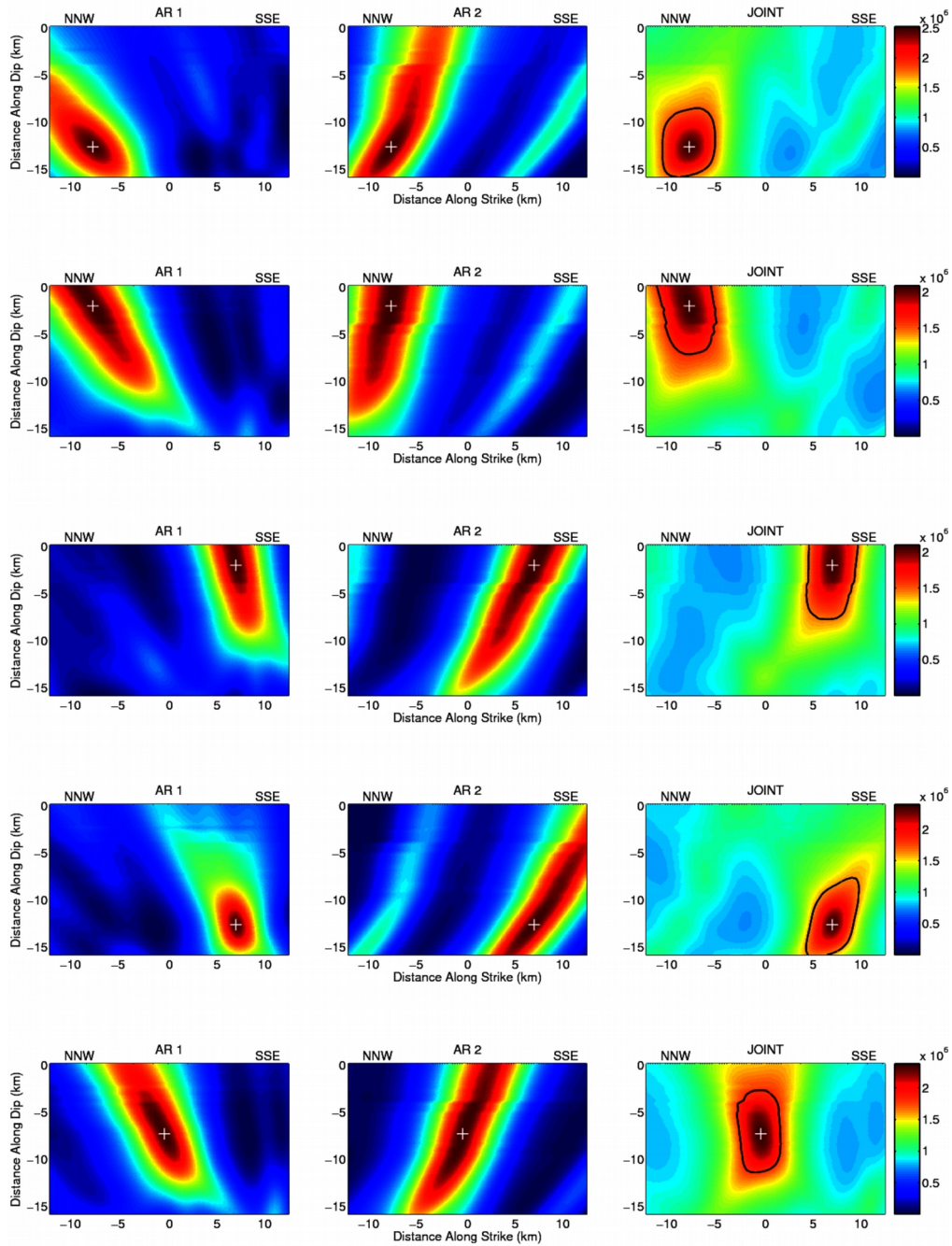


Figure 4 – Images of the beam power for a set of five synthetic sources (white crosses) positioned at different locations on the model fault plane. For each row, and from left two right, images refer to results from sub-array AR1, sub-array AR2, and the joint solution. Each source is analyzed separately; the dashed black lines bound those regions of the power spectra which are 1dB above the background spectral level.

The entire procedure is iterated over successive time frames, thus obtaining time-dependent images of the distribution of beam power over the modeled fault surface spanned by the synthetic sources X . The resolving capabilities of the method are tested using a set of five synthetic sources distributed at the center and corners of the model fault plane. The source time function is given by a 2-Hz Ricker wavelet, which is propagated across the two sub-arrays using the travel-time tables described earlier. Seismograms at individual stations are then contaminated by white, Gaussian noise with a signal-to-noise-ratio equal to 50, and processed using the same time window and frequency band as for the real case (see next Section). The different sources are analyzed separately, so that the obtained results do not account for interference phenomena associated with waves simultaneously issued by separate sources. Peaks of the synthetic BF spectra (Fig. 4) correctly recover the location of the different sources; in order to assess resolution, we follow Goldstein and Archuleta (1991b) and consider as significant only those $P(X)$ values which are 1dB above the background spectral level. This latter quantity is defined as two standard deviations above the mean of the BF spectrum. Resolution is on the order of ~ 7 km and ~ 5 km, respectively, along the down-dip and along-strike directions. In principle, the technique should thus be able to recover spatially-distinct point sources distributed throughout a fault surface whose inferred length and width are on the order of 20-25km and 5-15km, respectively (GdL INGV, 2016).

IV. RESULTS

BF power spectra are calculated over subsequent 2-s-long time windows shifting along

the seismograms with 1s increment. We limited the analysis to the first 5 seconds of signal, in order to avoid contamination by the S-wave arrivals. For each time frame, the power spectra obtained at the two sub-arrays are multiplied, so that the final back-projection image only contains the power contributions which are common to the two cluster of stations.

Over the first 1.5s of rupturing, spectra are dominated by radiation from the hypocentral area, with a slight up-dip propagation toward NNW. Within the 1.75s-2.25s time interval, bilateral rupture propagation becomes evident, with rupture fronts propagating up-dip toward SSE, and both up- and down-dip toward NNW. From the timing and location of those spectral peaks one gets rough estimates of rupture velocities in the 2.5-3.5 km/s range, which is consistent with the 3.1km/s inferred by Tinti *et al.* (2016) from full waveform inversion.

Time frames in between 2.75s and 3.75s are dominated by spectral peaks located NNW of the hypocenter, but at closer distances with respect to those observed at previous times. This apparent paradox, that would imply a retreat of the rupture front, can be interpreted in terms of the interference between waves simultaneously radiated by the previously-identified, separate rupture fronts expanding toward opposite directions.

V. DISCUSSION AND CONCLUSION

In this work we used back-projection of strong motion records to obtain a first estimate of rupture behavior during the early few seconds of the 2016, Mw=6.0, Central Italy earthquake. The reduced number of available stations, and their large relative distances hindered application of sophisticated, high-resolution methods.

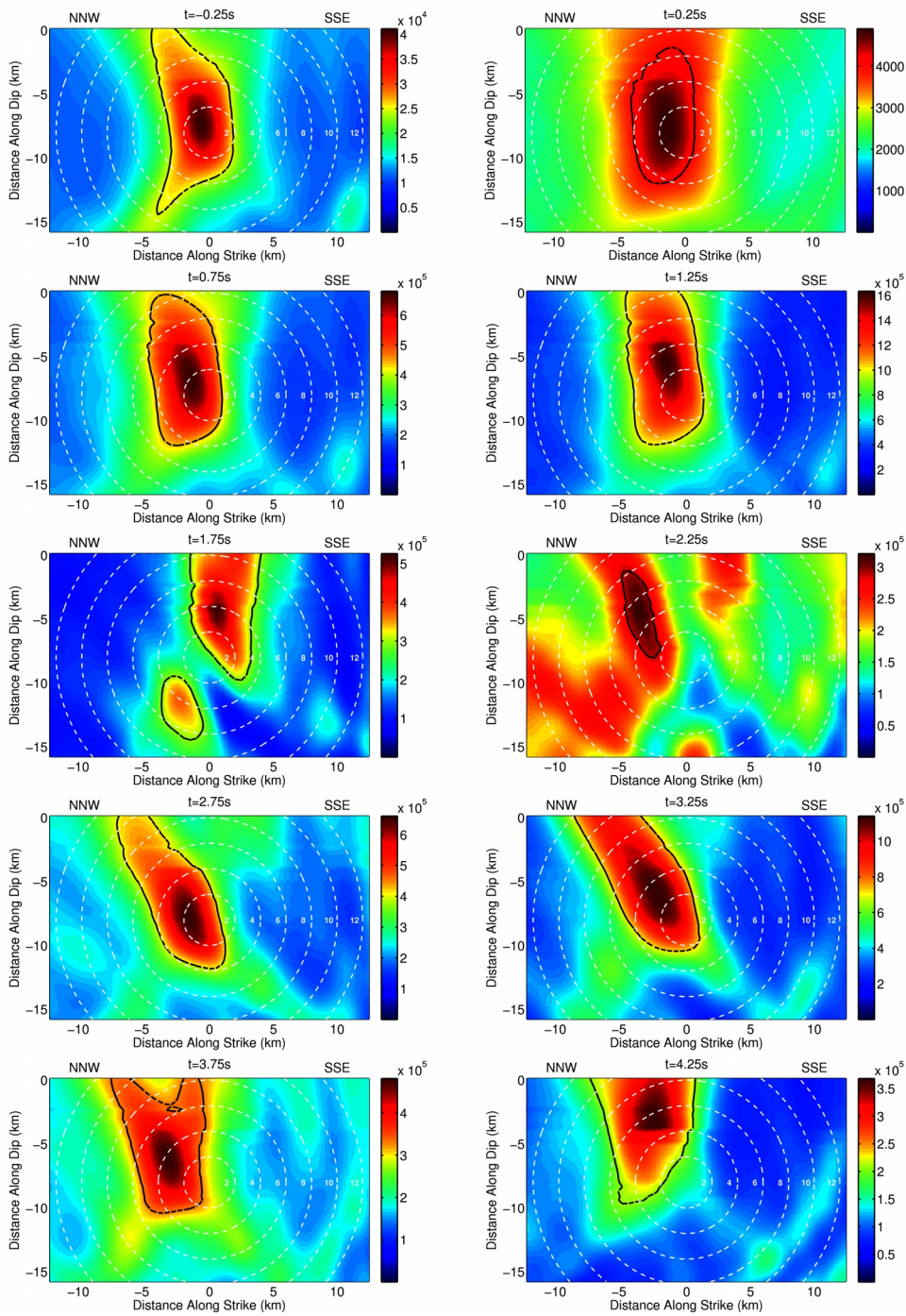


Figure 5 – Time dependent images of beam power over the model fault plane at subsequent time frames spaced by 0.5s. White, dashed circles are isolines of equal distance from the hypocenter.

As a consequence, our images are likely blurred by the interference of waves simultaneously radiated by distinct portions of the expanding rupture front. Nonetheless, the main features of the rupture history thus far presented are consistent with what reported by separate studies and observations. Our images indicate bilateral rupture, with peak energy radiations located SE updip and NW of the hypocenter. This is consistent with (a) the observed directivity focusing seismic energy mainly toward the N-NW as well as to the SE, as indicated by marked pulses in strong motion records (Tinti et al., 2016); (b) the spatial distribution of surface damages [GdL INGV, 2016], and (c) the pattern of co-seismic displacement. The overall picture is also in agreement with the results from waveform inversion of strong motion data by Tinti et al. (2016), who inferred heterogeneous slip distribution characterized by two shallow slip patches located up-dip and NW from the hypocenter, and bilateral rupture propagation with rupture velocity on the order of 3 km/s.

The simplicity of the processing steps presented in this note suggests the possibility of deploying multiple seismic arrays at close distances from seismogenic faults, aimed at the real-time tracking of rupture evolution in case of large earthquakes. This would provide a quick estimate of fault size and hence earthquake magnitude, contributing to the robustness of early-warning systems and rapid damage assessment.

DATA AND SHARING RESOURCES

Data are made available by the Italian Dipartimento della Protezione Civile - Presidenza del Consiglio dei Ministri (<http://ran.protezionecivile.it/>; last accessed Sept. 30, 2016).

ACKNOWLEDGEMENTS

Colleagues Elisa Tinti and Laura Scognamiglio are sincerely acknowledged for providing us with the submitted draft of their manuscript.

REFERENCES

- [Abrahamson and Bolt, 1987] Abrahamson, N.A., and B.A. Bolt, (1987). Array Analysis and Synthesis Mapping of Strong Seismic Motion. In *Seismic Strong Motion Synthetics*, Bruce A. Bolt (Editor). Academic Press, Orlando, Florida. 55-90.
- [Capon, 1969] Capon, J., (1969). High-resolution frequency-wavenumber spectrum analysis, *Proc. IEEE*, 57(8), 1408–1418.
- [Carannante *et al.*, 2013] Carannante, S., G. Monachesi, M. Cattaneo, A. Amato, and C. Chiarabba, (2013). Deep structure and tectonics of the northern-central Apennines as seen by regional-scale tomography and 3-D located earthquakes, *J. Geophys. Res.*, 118, 5391–5403, doi:10.1002/jgrb.50371.
- [Gal *et al.*, 2014] Gal, M., A. M. Reading, S. P. Ellingsen, K. D. Koper, S. J. Gibbons and S.P. Näsholm, (2014). Improved implementation of the fk and Capon methods for array analysis of seismic noise. *Geophys. J. Int.* 198, 1045–1054, doi: 10.1093/gji/ggu183
- [Goldstein and Archuleta, 1987] Goldstein, P., and R.J. Archuleta (1987). Array analysis of seismic signals. *Geophys. Res. Lett.*, 14, 13-16.
- [Goldstein and Archuleta, 1991a] Goldstein, P., and R. J. Archuleta (1991a), Deterministic frequency-wavenumber methods and direct measurements of rupture propagation during earthquakes using a dense array: Theory and methods, *J. Geophys. Res.*, 96(B4), 6173–6185, doi:10.1029/90JB02123.
- [Goldstein and Archuleta, 1991b] Goldstein, P., and R. J. Archuleta (1991b), Deterministic fre-

quency-wavenumber methods and direct measurements of rupture propagation during earthquakes using a dense array: Data Analysis, *J. Geophys. Res.*, 96(B4), 6187–6198.

[GdL INGV, 2016] Gruppo di Lavoro INGV (2016). Secondo rapporto di sintesi sul Terremoto di Amatrice Ml 6.0 del 24 Agosto 2016 (Italia Centrale). doi: 10.5281/zenodo.154400

[GdL IREA-CNR & INGV 2016] Gruppo di Lavoro IREA-CNR & INGV, (2016). Sequenza sismica di Amatrice: aggiornamento delle analisi interferometriche satellitari e modelli di sorgente, doi: 292 10.5281/zenodo.61682.

[Kiser and Ishii, 2012] Kiser, E., and M. Ishii, (2012). Combining seismic arrays to image the high-frequency characteristics of large earthquakes. *Geophys. J. Int.* 188, 1117–1128. doi: 10.1111/j.1365-246X.2011.05299.x

[Meng *et al.*, 2012] Meng, L., J.-P. Ampuero, A. Sladen, and H. Rendon (2012), High-resolution backprojection at regional distance: Application to the Haiti M7.0 earthquake and comparisons with finite source studies, *J. Geophys. Res.*, 117, B04313, doi:10.1029/2011JB008702.

[Rost and Thomas, 2002] Rost, S. and Thomas, C. (2002). Array seismology: methods and applications. *Rev. Geophys.*, 40, doi:10.1029/2000RG000100.

[Tinti *et al.*, 2016] Tinti, E., L. Scognamiglio, A. Michellini and M. Cocco (2016). Slip heterogeneity and directivity of the M L 6.0, 2016, Amatrice earthquake estimated with rapid finite-fault inversion. Submitted to *Geophys. Res. Lett.*